CHEMISTRY

Rapid sorting and auxiliary evaluation of malignant breast tumors by accurate imaging analysis of metastasis-related biomarker

Shan Zuo[1], Yanhua Li[1], Yushi Chen[2], Gangwei Jiang[1]*, Zhixuan Zhou[1], Tian-Bing Ren[1], Lanlan Chen[2], Sulai Liu[3], Shulin Huang[4]*, Xiao-Bing Zhang[1], Lin Yuan[1]*

Accurate differentiation of benign and malignant breast tumors is paramount for establishing schemes of breast cancer treatment and prognosis. Here we report a near-infrared (NIR) fluorescence probe (YF-1) with the overexpressed cathepsin C (CTSC) in metastatic breast tumors as the detecting substrate. This probe allows accurate identification of malignant tumor tissue specimens among tumor tissue specimens with unknown properties in a blind study. Importantly, a series of visible to NIR CTSC-activated fluorescence probes based on the same strategy realize effective identification of malignant tumor tissues, suggesting that CTSC could be the specific identification substrate of malignant breast tumors. Furthermore, a hydrophilic PEG moiety is coupled into YF-1, producing another CTSC-activated NIR probe (YF-2). YF-2 has excellent tumor-targeting capability, enabling the visualization of lung-metastatic breast tumors. The excellent detection accuracy and construction versatility of CTSC probes pave the way for preoperative diagnosis of malignant breast tumors.

INTRODUCTION

Tumors are serious threats to human health and have become the leading cause of mortality (*1*, *2*). In various types of tumors, breast tumors are at the forefront of morbidity and mortality among females (*3*). Breast tumors can be classified into benign and malignant tumors based on the phenotypic appearance, tumor size, and stage. Generally, benign breast tumors grow slowly and have clear boundaries and regular morphology. Malignant breast tumors display the rapid rate of growth and phenotypic appearance over benign breast tumors and have a lot of pseudopods to erode the normal glands, which endow it with a high metastatic potential (*4*). Notably, more than 90% of breast cancer mortalities are caused by metastasis (*5*–*7*). Clinically, the breast tumors enlarge rapidly over a short period due to the transformation of tumor's characteristics from benign into malignant (*8*). Therefore, identification of the tumor's characteristic (benign/malignancy) is of great concern for the early and accurate diagnosis of breast tumors (*9*, *10*).

Until now, some medical imaging techniques have been applied for the diagnosis of breast cancers, including magnetic resonance imaging, positron emission tomography, x-ray computed tomography, ultrasound, and so on (*11*–*13*). These techniques can visualize the location and size of tumors but are difficult to provide tumor's characteristic. The clinical diagnosis of malignant breast tumors mainly relies on the needle biopsy, which is a time-consuming and painful process (*14*–*16*). Moreover, needle biopsy could induce implant metastasis and cannot map the metastasis extent of malignant breast tumors (*17*). As a crowded topic in recent years, fluorescence probe–based imaging techniques have made great strides in the early diagnosis of diseases by virtue of their unique merits including no radiation exposure, noninvasiveness, high sensitivity, and real-time imaging (*18*–*25*). On account of the abnormal biomolecular content/activity {reactive species [reactive oxygen (ROS), reactive nitrogen (RNS), and reactive sulfur (RSS)] and enzymes} and microenvironments (pH, polarity, and viscosity) in tumors, researchers have developed numerous fluorescence probes to diagnosis and imaging tumors (*26*–*31*). Nonetheless, small differences of these abnormal indexes between benign and malignant tumors have made it difficult to reveal the carcinogenic characteristics of tumors.

Cathepsins, a class of enzymes that degrade proteins, are present in all animals and other organisms and play an important role in maintaining cellular homeostasis. Categorized by their structure and catalytic mechanism, there are more than a dozen members in this enzyme family (*32*–*34*). Among these members, Cathepsin C (CTSC) has been confirmed to be strongly associated with breast cancer metastasis to the lung, while there is no obvious significance to primary tumor growth (*35*). Clinical research has indicated that high CTSC activity was associated with an increased incidence of brain and lung metastases and low survival of patients with breast cancer (*36*). Further studies revealed that CTSC had higher activity in metastatic tumors over primary tumors, and CTSC promoted cancer cell proliferation in the lungs at an early stage of breast cancer metastasis (fig. S1). (*37*). Considering that metastasis is an outward manifestation of malignancy, we speculated that CTSC might be a potential candidate for identifying carcinogenic characteristics of tumors.

We here report a near-infrared (NIR) fluorescence (NIRF) probe (YF-1) responsive to CTSC for specifically diagnosing and imaging malignant breast tumors (Fig. 1). YF-1 successfully diagnosed the malignancy of different types of homologous cancer cells and demonstrated that murine 4T1 cells and humanized MDA-LM2 cells had higher invasiveness than other cancer cells. Furthermore, YF-1 efficiently differentiated malignant tumor tissues and benign tumor or lump tissues in mice models. More notably, YF-1 could accurately

[1]State Key Laboratory of Chemo and Biosensing, College of Chemistry and Chemical Engineering, Hunan University, Changsha, 410082, China. [2]MOE Key Laboratory for Analytical Science of Food Safety and Biology, Fujian Provincial Key Laboratory of Analysis and Detection Technology for Food Safety, College of Chemistry, Fuzhou University, Fuzhou, 350108, China. [3]Department of Hepatobiliary Surgery/Central Laboratory, Hunan Provincial People's Hospital (The First Affiliated Hospital of Hunan Normal University), Changsha, 410005, China. [4]Department of Breast and Thyroid Surgery, Hunan Provincial People's Hospital (The First Affiliated Hospital of Hunan Normal University), Changsha, 410005, China.
*Corresponding author. Email: jianggangwei@hnu.edu.cn (G.J.); slhuang369@hunnu.edu.cn (S.H.); lyuan@hnu.edu.cn (L.Y.)

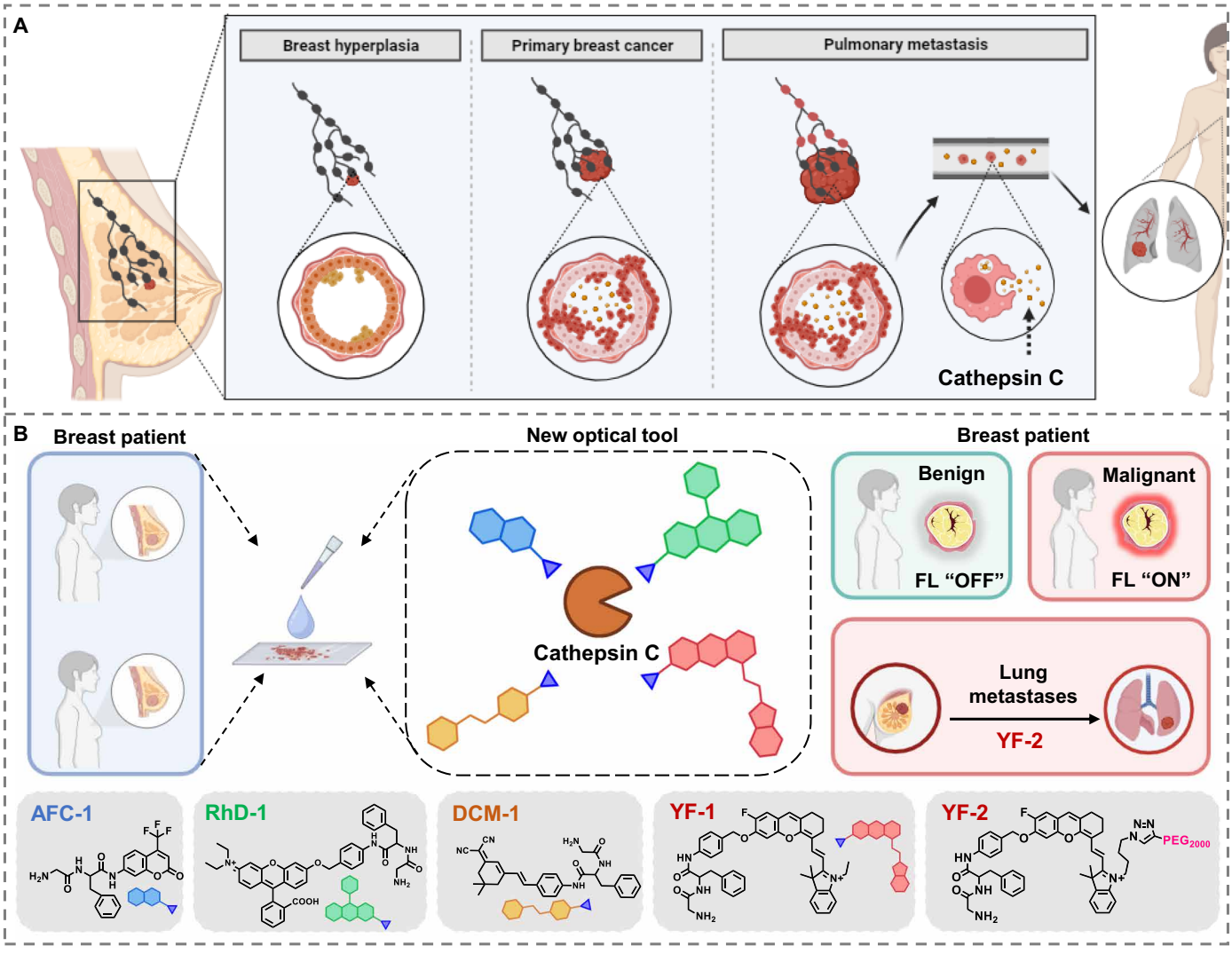

Fig. 1. Design and mechanisms of YFs for specific diagnosis and imaging of malignant breast tumors. (**A**) Associated schematic of CTSC and lung metastasis of malignant breast cancer. (**B**) Illustration of CTSC-activated fluorescence probe based on different wavelength fluorophore for diagnosis of malignant breast cancer.

and rapidly identify malignant breast tumor tissues of patients with malignant breast cancer in a blind study. Furthermore, we extended the CTSC recognition site to other dye skeletons and constructed a series of visible to NIR fluorescence probes. All of these probes displayed excellent capability for identifying malignant breast tumor tissues, suggesting that CTSC could be the specific identification substrate of malignant breast tumors. In addition, decorating YF-1 with a hydrophilic PEG moiety (YF-2) alleviated the enrichment of the probe in the liver and improved the tumor-targeting capability of the probe, enabling the visualization of breast cancer metastases to the lung.

RESULTS

Synthesis and characteristics

To avoid the disturbance of autofluorescence of tissues and to visualize CTSC in deep tissues, we applied fluorine substituted hemicyanine dye (HDF-1) with NIR absorption and emission maximum as fluorescent reporting moiety (*38*). A fluorine atom was introduced into the ortho-position of hydroxyl group to regulate pK_a (where K_a is the acid dissociation constant) value, allowing HDF-1 to deprotonate in the tumor microenvironment and transform into zwitterionic form with strong fluorescence (*39*). Probe YF-1 was designed through coupling HDF-1 with CTSC-cleavable peptide, glycine-phenylalanine (Gly-Phe), via a self-immolative linker, para-aminobenzylalcohol (PABA) (Fig. 2A) (*40*).

After obtaining dye HDF-1 and probe YF-1, we first explored their optical/chemical properties in aqueous solution. At physiological pH, YF-1 and HDF-1 showed the absorption maximum at 610/660 and 695 nm, respectively. Excited by a laser of 650 nm, HDF-1 displayed strong fluorescence at 715 nm, while weak fluorescence was observed in aqueous solution containing YF-1 (fig. S2). The fluorescent intensity ratio of HDF-1 and YF-1 is 50.0-fold, indicating that the introduction of CTSC identification site significantly quenched the fluorescence of HDF-1. YF-1 showed a weak and stable fluorescence signal at 715 nm in buffer solvent with different pH

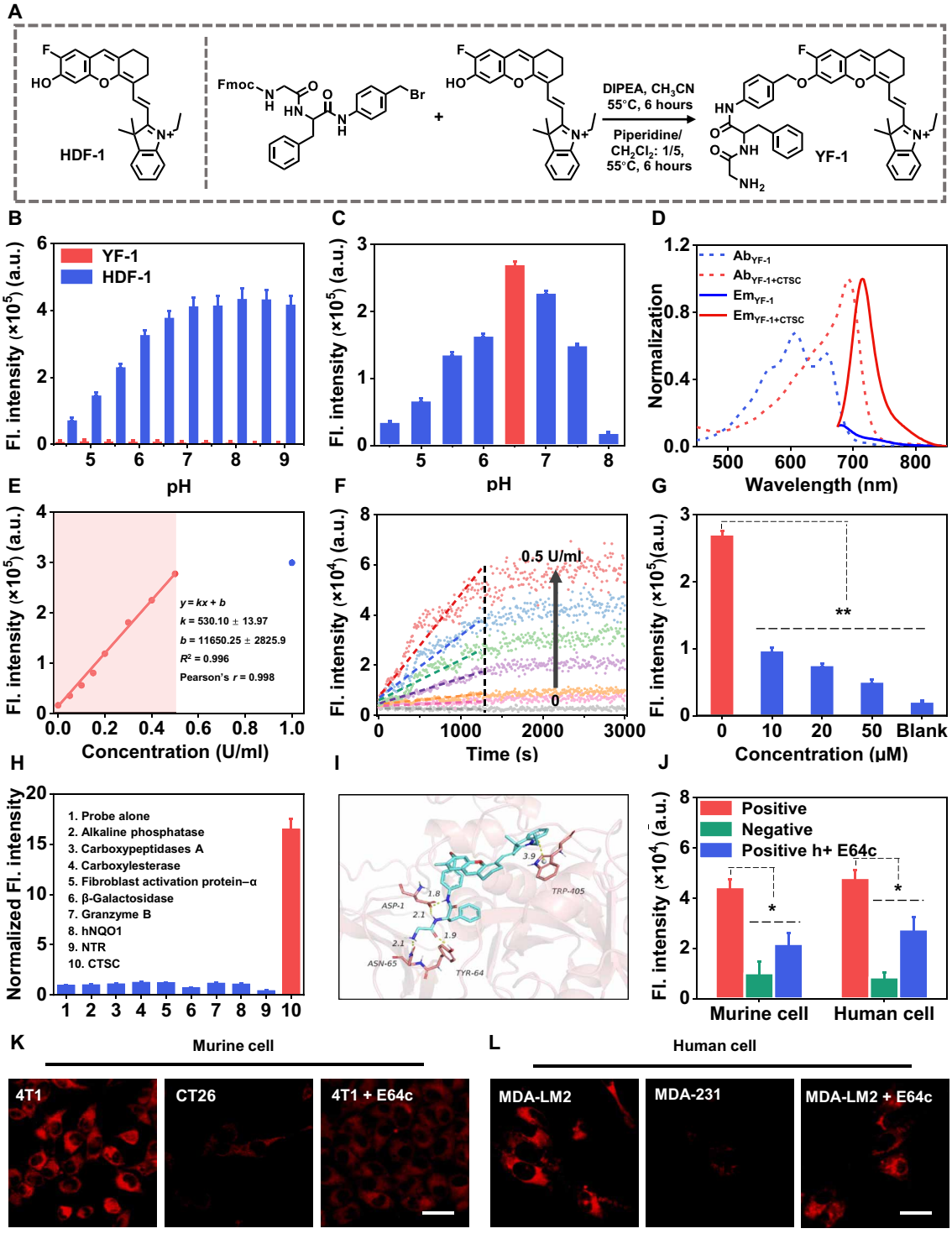

Fig. 2. Synthesis and in vitro evaluation of YF-1. (**A**) Structures of HDF-1 and synthesis of YF-1. The specific synthesis methods are displayed in Supplementary Materials. (**B**) Fluorescence intensity at 715 nm of YF-1 (5 μM) and HDF-1 (5 μM) in MES buffers. (**C**) Fluorescence intensity at 715 nm of YF-1 (5 μM) after incubation of with CTSC (0.5 U/ml) in MES buffers (pH 4.0 to 8.0). (**D**) Normalized absorption spectra (dotted line) and fluorescence spectra (solid line) of YF-1 (5 μM) in the absence or presence of CTSC (0.5 U/ml) in MES buffer (pH 6.5) at 37°C. (**E**) Linear fitting curve of YF-1 (5 μM) at 715 nm against CTSC. (**F**) Time-dependent response of YF-1 (5 μM) to CTSC with different concentrations (0 to 0.5 U/ml). (**G**) Fluorescence intensity of YF-1 at 715 nm in the presence of CTSC (0.5 U/liter) and E-64c (loxistatin acid, a CTSC inhibitor) with different concentrations (0 to 50 μM). (**H**) Normalized fluorescence intensities of YF-1 (5 μM) in the presence of various biomolecules. (**I**) Predicted conformation of CTSC–YF-1 complex. (**J**) Quantitative fluorescence intensities of cells in (K) and (L). (**K** and **L**) Fluorescence imaging of murine cancer cells (K) and human cancer cells (L) incubated with YF-1 (5 μM) in the absence and presence of CTSC inhibitor (E-64c, 50 μM). Scale bars, 40 μm. Error bars, ± SEM. $n = 3$ for (B), (C), (E), (G), and (H); $n = 5$ for (J). $^{*}P < 0.05$ and $^{**}P < 0.01$. a.u., arbitrary unit.

(4.5 to 9.0), while HDF-1 exhibited the increasing fluorescence intensity at 715 nm as pH rose from 4.5 to 7.0 (Fig. 2B). Notably, the probe presented the strongest fluorescence intensity at pH 6.5 when exposed to CTSC (Fig. 2C and fig. S3). These results suggested that CTSC had the best activity in weak-acid environment, which was consistent with the reported reference (*34*). Therefore, we examined in detail the capability of YF-1 to detect CTSC in aqueous solution of pH 6.5. Upon the addition of CTSC, YF-1 displayed an obvious fluorescence enhancement (15-fold) at 715 nm, accompanied by red-shift and increase of absorption maximum (Fig. 2D). The fluorescence intensity of YF-1 presented a linear relationship with the CTSC activity from 0 to 0.5 U/ml (Fig. 2E and fig. S4). Meanwhile, YF-1 could achieve fluorescence equilibrium faster as CTSC activity increased (Fig. 2F). The calculated detection limit and enzymatic Michaelis-Menten constant (K_m) of YF-1 were 0.022 U/ml and 2.99 μM, respectively. The catalytic rate constant (k_{cat}) and catalytic efficiency (k_{cat}/K_m) of CTSC were determined to be 0.377 s^{-1} and 7.93×10^6 M^{-1} s^{-1}, respectively (fig. S5). YF-1 was then incubated with CTSC in the presence or absence of loxistatin acid (E-64c), a CTSC inhibitor (*41*). The turn-on fluorescence of YF-1 gradually weakened with increasing concentrations of E-64c (Fig. 2G and fig. S6). YF-1 displayed negligible increases of fluorescent intensity upon incubation with the homologous family enzymes (cathepsin B, D, K, and S) and other types of enzymes (Fig. 2H and figs. S7 and S8). These results demonstrated that YF-1 had excellent detection specificity and selectivity toward CTSC, which also prompted us to further investigate the interaction between YF-1 and CTSC at the molecular level. The docking data showed that the distances of YF-1 and active sites of CTSC (Asp^1, Asn^{65}, and Tyr^6) are 1.8, 2.1, and 1.9 Å, respectively, smaller than the 3.5 Å of the traditional hydrogen bonding, which suggested that strong hydrogen bonding interactions existed between YF-1 and CTSC. Meanwhile, a strong π-π conjugation interaction between YF-1 and Trp^{405} amino acid was observed, revealing that YF-1 could form stable complexes with CTSC, which could be the primary cause for excellent detection specificity and selectivity of YF-1 toward CTSC (Fig. 2I) (*42*).

We then applied YF-1 to detect intracellular CTSC activity after confirming its inappreciable cytotoxicity (fig. S9). Cancer cells preincubated with E-64c displayed weaker fluorescence signals than untreated cancer cells (Fig. 2, J to L), indicating that YF-1 could detect the intracellular CTSC activity (fig. S10). Notably, 4T1 cells with high metastasis risk displayed stronger fluorescence signal after incubation with YF-1 than CT26 with low metastasis risk (*43*). The similar results had been observed in human cancer cells (triple-negative breast cancer cells (MDA231) and screen-purified breast cancer cells with high metastasis risk (MDA231-LM2)) (Fig. 2L). The scratch test exhibited that E-64c could inhibit the migration of 4T1 cells (fig. S11). These results confirmed the existence of a positive correlation between CTSC activity and tumor metastasis (Fig. 2K). In addition, we further applied YF-1 to incubate 4T1 cells (cancer cells), human embryonic kidney (HEK) 293 cells (normal cells), and the mixed cells. As shown in fig. S12, the fluorescence intensity of 4T1 cells was obviously stronger than that of HEK293 cells, suggesting that the activity of CTSC in 4T1 cells was higher than that in HEK293 cells. Meanwhile, the fluorescence brightness of the both cells in the mixed state was similar with that in the single culture state, which indicated that mixed culture insignificantly change the activity of CTSC in 4T1 cells and HEK293 cells. These results demonstrated that YF-1 had the capability to judge the aggressiveness of cancer cells and distinguish 4T1 cells with high metastasis risk from other cells through detecting endogenous CTSC activity.

In situ distinction between organizations of different properties

Inspired by the results of the in vitro tests, we further applied YF-1 to detect CTSC activity in vivo. 4T1 tumors injected intratumorally, with YF-1 displayed stronger fluorescence signals than subcutaneous tissues over 10 hours (fig. S13). Moreover, the signal intensity ratio between tumor and subcutaneous tissues had increased to 4.8-fold at 15 min post-injection, indicating that YF-1 could be activated by the overexpressed CTSC in 4T1 tumors (fig. S13). Further, YF-1 was indiscriminately sprayed on cancerous and paraneoplastic tissues (Fig. 3A and fig. S14). The fluorescence signals of 4T1 tumors gradually increased over 30 min, while skin and muscle tissues remained weak signals (Fig. 3, A and B). Signal intensity ratio between tumor and paraneoplastic muscle tissues was 10.0-fold (Fig. 3, C and D). Subsequent hematoxylin and eosin (H&E) staining demonstrated morphological differences of the tumor and paraneoplastic muscle tissues (Fig. 3E), which validated that YF-1 could be an excellent imaging tool for distinguishing cancerous and paraneoplastic tissues, and it had the potential to be applied for fluorescence-guided surgery.

It is of great significance for the early treatment of cancers to assess the carcinoma characteristics of tumors (benign or malignancy) in a timely manner (*44*, *45*). Probe YF-1 might be able to resolve the current dilemma due to CTSC overexpression in malignant tumors with high metastasis. YF-1 was intratumorally injected into tumors with different metastatic capabilities, including C6 (glioma, essentially no metastases), CT26 (colorectal cancer, multiple proximal metastases), and 4T1 (mammary carcinoma, multiple distal metastases) tumors (fig. S15). Fluorescence signals of 4T1 tumors increased over time and reached more than eightfold enhancement at 1 hour post-injection, while there was no significant fluorescence increase to be observed in C6 and CT26 tumors (Fig. 3F). The fluorescence signal ratio of 4T1 tumors and C6/CT26 tumors was calculated to be 7.1-fold and 6.3-fold, respectively (Fig. 3G). A similar phenomenon was also observed in the isolated tumors (Fig. 3, H and J). Furthermore, we lysed tumor tissues and separated proteins by SDS–polyacrylamide gel electrophoresis. Higher expression contents of CTSC were observed in 4T1 tumor lysates over CT26 and C6 tumor lysates (Fig. 3I), confirming that the fluorescence enhancement of YF-1 is directly related to overexpressed CTSC in 4T1 tumor.

Precisely diagnosing benign/malignant breast tissues of mice and human

Recognizing the benign and malignant features of tumors is of broad social concern and was related with cancer treatment and prognosis. To achieve this goal, modern physicians often apply a combination of pathological biopsy and imaging, which increases the demands for imaging instruments and pathology analysts (*46*–*51*). YF-1 might be qualified for this task considering its superior performance for detecting CTSC. Malignant breast cancer (in situ 4T1 tumors) and benign breast lesions (breast hyperplasia) were selected to examine the capability of YF-1 for diagnosing the malignant tumors. The two models were constructed by the implantation of 4T1-Luc cells in breast pads for 10 days and feeding estrogen for 25 days, respectively (Fig. 3K). Some distinct features of malignant tumors were observed in the H&E staining, such as irregular cellular

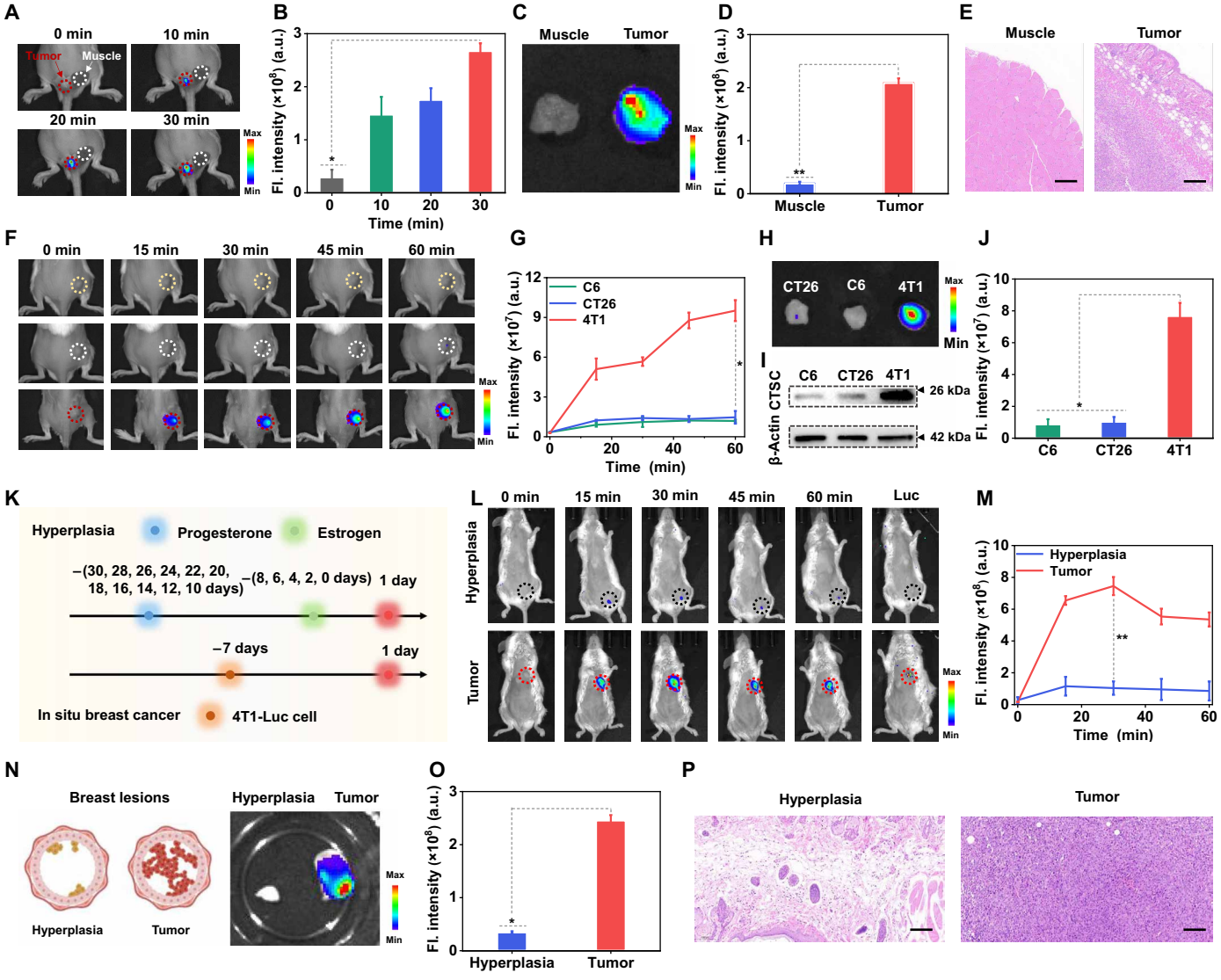

Fig. 3. Application of YF-1 in identifying cancer characteristics of mouse models. (**A** and **C**) In vivo (A) and in vitro imaging (C) of tumor and muscle tissues sprayed with YF-1 (20 μM). (**B** and **D**) Quantitative fluorescence analysis of YF-1 in in vivo (A) and in vitro imaging (C). (**E**) H&E staining of muscle and tumor tissues. Scale bars, 100 μm. (**F**) Real-time-fluorescence imaging of Balb/c mice bearing C6 tumors (top), CT26 tumors (middle), and 4T1 tumors (down), respectively, after intratumoral injection of YF-1 (200 μM, 30 μl). (**G**) Dynamic fluorescence intensities of tumors in (F). (**H**) Representative fluorescence images of the isolated tumors (C6, CT26, and 4T1 tumors) after intratumoral injection of YF-1 (200 μM, 30 μl). (**I**) Western blot of CTSC and β-actin in C6, CT26, and 4T1 tumor lysates. (**J**) Quantitative fluorescence intensity of isolated tumor tissues in (H). (**K**) Schematic illustration of establishing the breast hyperplasia and breast cancer mouse models. (**L**) Representative fluorescence images of the mice with breast hyperplasia (top) and tumors (down) after directly injecting YF-1 (200 μM, 30 μl) into the lesions. (**M**) Dynamic fluorescence intensities of tumors in (L). (**N**) Representative fluorescence images of isolated tumor and breast hyperplasia tissues after injection of YF-1 (200 μM, 30 μl). (**O**) Quantitative fluorescence intensity of isolated tissues in (N). (**P**) H&E staining of the breast hyperplasia tissues and 4T1 tumor tissues. Scale bars, 200 μm. Error bars, ± SEM. $n = 3$. $^{*}P < 0.05$ and $^{**}P < 0.01$.

arrangement and abnormal nuclear morphology, while there were the marked ductal structures in breast hyperplasia tissues (Fig. 3P), indicated that the two models were successfully established. Imaging was performed after in situ injection of YF-1 (Fig. 3L, left). The fluorescent signals in the 4T1-Luc tumors reached a maximum after 30 min post-injection and were 4.5-fold higher than that in breast hyperplasia (Fig. 3M). The bioluminescent signal carried by 4T1-Luc cells also appeared only in mice bearing breast tumors (Fig. 3L, right). A similar phenomenon was observed in the isolated tumors and hyperplasia tissues (Fig. 3, N and O), which was reconfirmed by Western blot analysis of CTSC (fig. S16), indicating that YF-1 could precisely diagnose the malignant tumors.

We further applied YF-1 for diagnosing the malignant tumor tissues of human from benign ones in a blind study (Fig. 4A). The surgical tissue specimens from 14 patients with benign or malignant breast cancer were harvested, cryo-sectioned into 20 μm in thicknesses, and then incubated with YF-1 for 20 min, followed by imaging. As shown in Fig. 4B, seven breast tissue specimens (#1 to #7) showed a stronger fluorescence signal (10-fold) over the other seven specimens (#8 to #14) (Fig. 4, B and C), indicating that there was the

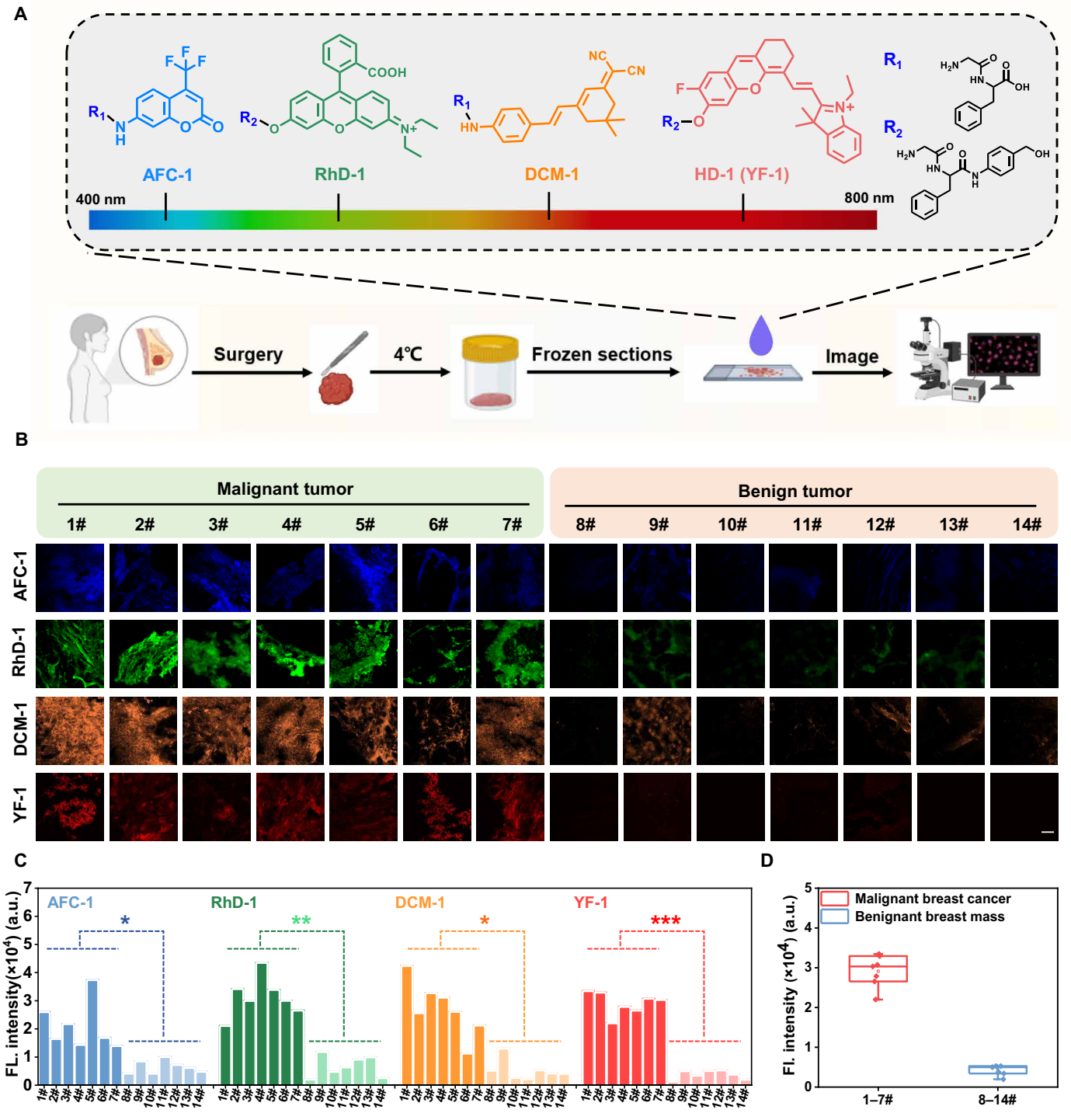

Fig. 4. Application of YF-1 in identifying cancer characteristic of human breast cancer tissues. (**A**) Schematic illustration of sample preparation and fluorescence analysis of human breast cancer tissues. Dotted box: Chemical structure of four CTSC-activated fluorescent probes spanning visible to NIR light region based on other dye skeletons. (**B**) Confocal fluorescence images of tissue sections harvested from surgical specimens of seven possible breast cancer patients (left) and seven possible other breast disease patients (right) after incubation with the four probes (AFC-1, RhD-1, DCM-1, and YF-1) (20 μM, 20 min), respectively. Scale bar, 40 μm. (**C**) Quantitative fluorescence intensity of frozen sections in (B). (**D**) Box plots of two test specimen groups. *$P < 0.05$, **$P < 0.01$, and ***$P < 0.001$.

higher CTSC activity in the first seven tissue specimens over the last seven tissue specimens. Considering the correlation between CTSC activity and tumor characteristics, we speculated that #1 to #7 and #8 to #14 were patients with malignant breast cancer and patients with benign breast cancer, respectively. Unexpectedly, the subsequent H&E staining and clinical diagnosis confirmed this conjecture (Fig. 4D, fig. S17, and table S1). H&E staining exhibited that there were obvious malignancy features in #1 to #7 tissue specimens, large numbers of nuclei with elongated peripheral infiltration lines, while the benign tumor features, including the regular and rounded tumor morphology and the clear isolation between tumor and adjacent tissues, were observed in #8 to #14 tissue specimens (fig. S17) (*52*, *53*). These astonishingly consistent results indicated that YF-1 could accurately diagnose malignant tissues. In addition, clinical diagnosis reports presented that there was lymphatic metastasis with varying degrees in 1#, 2#, and 4# to 7# tumor tissue specimens while that was not obviously observed in 3# specimens (table S1), which might be responsible for the significantly low fluorescence intensity in 3# tissue specimens (Fig. 4B). These results demonstrated the clinical promise of YF-1 for the diagnosis of malignant metastatic breast tumors.

Subsequently, we extended CTSC identification site to other dye skeletons [coumarin, rhodol, and dicyanomethylene-4H-pyran chromophores (DCM)], and constructed a series of CTSC-activated fluorescent probes (AFC-1, RhD-1, and DCM-1) spanning visible to NIR light region (Fig. 4A and figs. S18 to S20). These probes could be quickly activated by CTSC, and then emit fluorescence (figs. S18 to S20). All of these probes could effectively identify malignant breast tumors in a blind study, which suggested that CTSC could be the specific identification substrate of malignant tumors (Fig. 4, B and C, and figs. S18D, S19D, and S20D). In addition, many fluorescent probes have also been developed to diagnose and image tumors by detecting other biomarkers, such as β-galactosidase (β-Gal) and hNOQ1 (*39*, *46*). On the basis of the merocyanine skeleton, we synthesized two probes (RX-2 and CS–β-Gal) and then used them for diagnosing the benign/malignant breast tissues of humans (fig. S22, A and C) (*39*, *54*, *55*). As shown in fig. S22, inapparent statistics differences of fluorescence signals were observed between malignant breast tumor tissues and benign ones incubated with RX-2 or CS–β-Gal. The disordered fluorescence signals in different human tissues suggested that there could be great heterogeneity of hNQO1 and β-Gal content. The remarkable performance of these CTSC-activated probes under the same scenario and imaging conditions suggested that CTSC could be a specific biomarker of malignant tumors once again.

Visualization of breast cancer lung metastasis

High invasiveness is an important feature of malignant tumors and often causes tumors to metastasize to other organs. Ultimately, this will result in multiple organ failures or even death (*56*). Visualization of tumor metastasis enables us to understand and timely control the development of malignant tumors (*57*–*60*). Considering the above superior performance of YF-1, we speculated that YF-1 might be applied for noninvasive and real-time imaging of metastases. Unfortunately, YF-1 was difficult to be activated in the tumors when injected via the tail vein (fig. S23). This could be related to the good lipophilicity (YF-$1_{Po/w}$ = 2.193, HDF-$1_{Po/w}$ = 2.452) and short circulation time ($t_{1/2}$ = 45 min), further resulting in the probe accumulating mainly in the liver, rather than in the tumor (figs. S24 to S26). To break through this bottleneck, we tried to introduce polyethylene glycol, molecular weight 2000 (PEG-2000) into HDF-1 and YF-1 to expand the hydrophilicity and circulation time and synthesized dye HDF-2 and probe YF-2 (Fig. 5A) (*61*). HDF-2 and YF-2 spontaneously assembled spherical nanoparticles with an average hydrodynamic diameter of 30 nm in aqueous solution (Fig. 5, B and F) due to their amphipathic skeletons (hydrophobic merocyanine skeletons and hydrophilic PEG-2000) (*62*).

Consistent with our expectations, the introduction of hydrophilic PEG-2000 significantly relieved the lipophilicity (YF-$2_{Po/w}$ = 0.274, HDF-$2_{Po/w}$ = 0.320) and extended circulation time ($t_{1/2}$ = 200 min) (fig. S25). Furthermore, we explored the pharmacokinetics of YFs. HDF-1 and HDF-2 were injected into mice via the tail vein, respectively. The main organs (heart, liver, spleen, lung, and kidney) were acquired after 30 min, followed by imaging. Compared to HDF-1, HDF-2 containing PEG-2000 displayed significantly reduced fluorescence signal in the liver and enhanced fluorescence signals in other organs, which was conductive to the detection of CTSC activity in metastatic tumors (fig. S27). Considering that 4T1 tumors are susceptible to lung metastasis, we performed whole-body longitudinal NIRF imaging of the mice at different time points post-injection (0, 5, 15, 30, and 60 min) and detailly studied the enrichment of both dyes in lungs. Stronger NIR fluorescence signals were observed in the lungs (dorsal views) of mice treated by HDF-2 over that of mice treated by HDF-1 at every time point post-injection (3 to 30 min) (Fig. 5J). The recorded fluorescence signal of HDF-2 was strongest after 9 min post-injection, producing a sevenfold fluorescence enhancement (Fig. 5G). Therefore, driven by these observations, we expected that probe YF-2 could be suitable for detecting CTSC in 4T1 lung-metastasis tumors.

Similar to YF-1, YF-2 showed a 15-fold fluorescence increase at 715 nm after co-incubation with CTSC (0.5 U/ml) and reached maximum fluorescence intensity when the incubation time was 30 min (Fig. 5, C and D). Fluorescence imaging further revealed the close responsiveness of YF-1 and YF-2 (Fig. 5E). These results indicated that the self-assembly produced a negligible effect on the responsiveness of the probe. We then applied YF-2 for offline (blood)/online (in vivo) diagnosis of lung metastasis progressions of breast cancer. After injection of 5×10^5 4T1-Luc cells or phosphate-buffered saline (PBS) (equal volume) via the tail vein, blood was obtained from the orbit vein at different time points, followed by serum extraction (Fig. 6A). The CTSC activity in serums was evaluated after incubation with YF-2 for 1 hour. The serum from metastatic mice showed significantly stronger fluorescence signals over that from normal mice. At days 3, 7, 10, and 14 post-injection of 4T1-Luc cells, the signal ratios between metastatic mice and normal mice in serums were 1.74-fold, 2.26-fold, 2.61-fold, and 2.50-fold, respectively (Fig. 6, C and D). This demonstrated that breast cancer metastasis was accompanied by an up-regulation of CTSC activity in serum (*37*). Next, to further explore the association of breast cancer lung metastasis and CTSC activity, we injected YF-2 into mice models with metastatic tumors (15 days) via the tail vein and performed noninvasive in vivo imaging (*37*, *63*). The lungs of mice bearing metastatic tumors displayed gradually enhanced fluorescence signals with the extension of time, while no obvious signal changes were observed in that of normal mice. YF-2 exhibited the strongest fluorescence signals in the lungs of mice bearing metastatic tumors at 90 min post-injection, which was 3.78-fold higher than in that of normal mice (Fig. 6, E and F). Naked eye observation

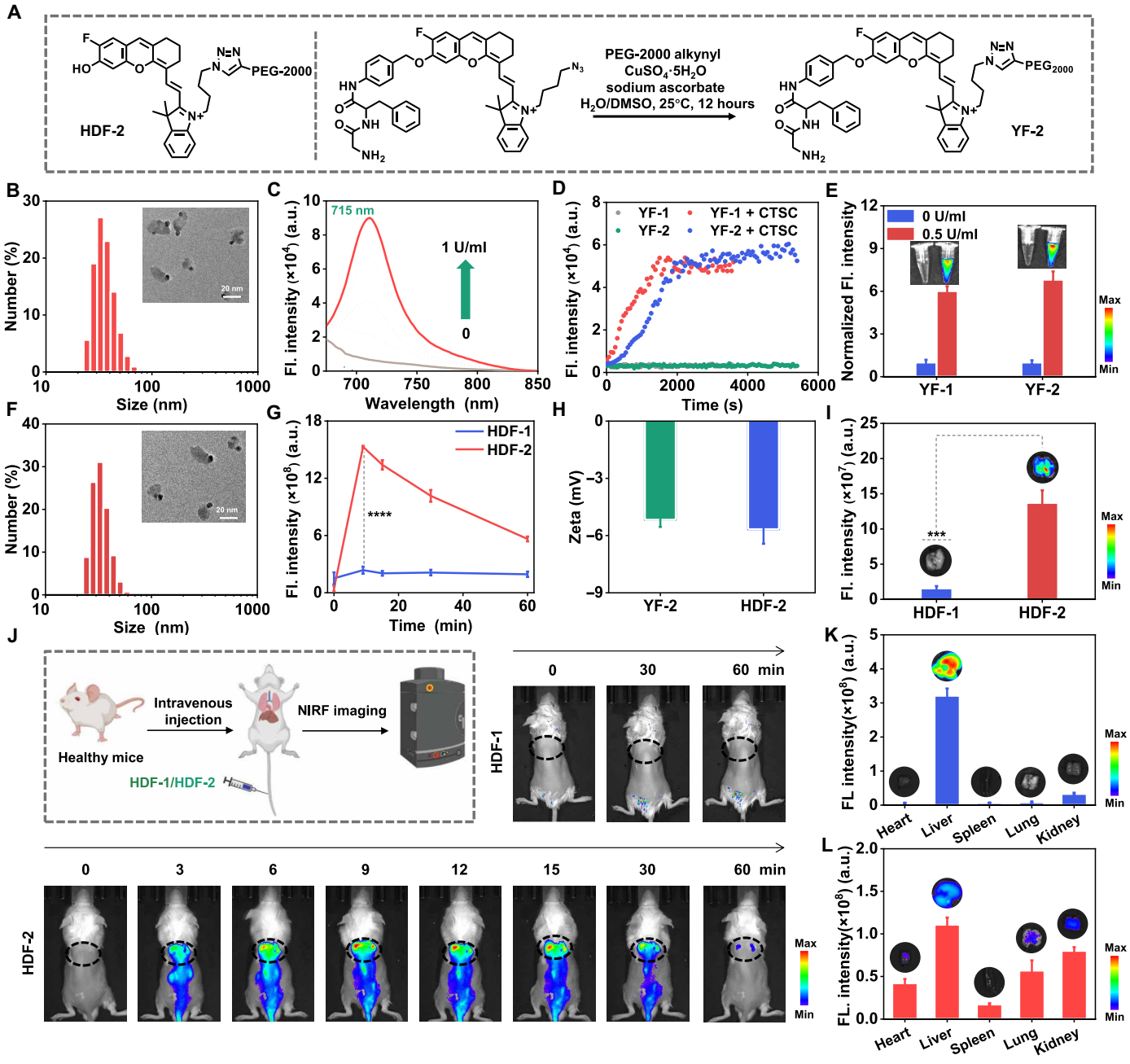

Fig. 5. Synthesis and lung accumulation studies of YF-2 and HDF-2. (**A**) Structures of HDF-2 and synthesis of YF-2. (**B** and **F**) DLS size distribution of YF-2 (B) and HDF-2 (F). Inset: Representative transmission electron microscopy images of YF-2 (B) and HDF-2 (F) in MES buffer. (**C**) Fluorescence spectra of YF-2 (5 μM) after incubation with CTSC (0 to 1 U/ml) in MES buffer for 30 min. (**D**) Time-dependent response of YF-1 and YF-2 in the absence or presence of CTSC (0.5 U/ml). (**E**) Normalized fluorescence intensity of YF-1 or YF-2 (5 μM) at 715 nm in the absence or presence of CTSC (0.5 U/ml) in MES buffer for 30 min. Inset: Fluorescence images of YF-1 and YF-2. (**G**) Quantitative fluorescence intensities of lungs in (J). (**H**) Zeta potential of YF-2 and HDF-2 in MES buffer. (**I**) Quantitative fluorescence intensities of isolated lung tissues after injection of HDF-1 or HDF-2 (200 μM, 100 μl). Inset: Fluorescent images of isolated lung tissues in (J). (**J**) Real-time fluorescence images of mice after intravenous injection of HDF-1 or HDF-2 (200 μM, 100 μl). Ex vivo fluorescence images and signal quantification of resected organs from mice at $t = 1$ hour intravenous injection of (**K**) HDF-1 and (**L**) HDF-2 (200 μM, 100 μl), respectively. Inset: In vitro imaging of major organs with different dyes in (A) and (B). Error bars, ± SEM. $n = 3$. ***$P < 0.001$ and ****$P < 0.0001$.

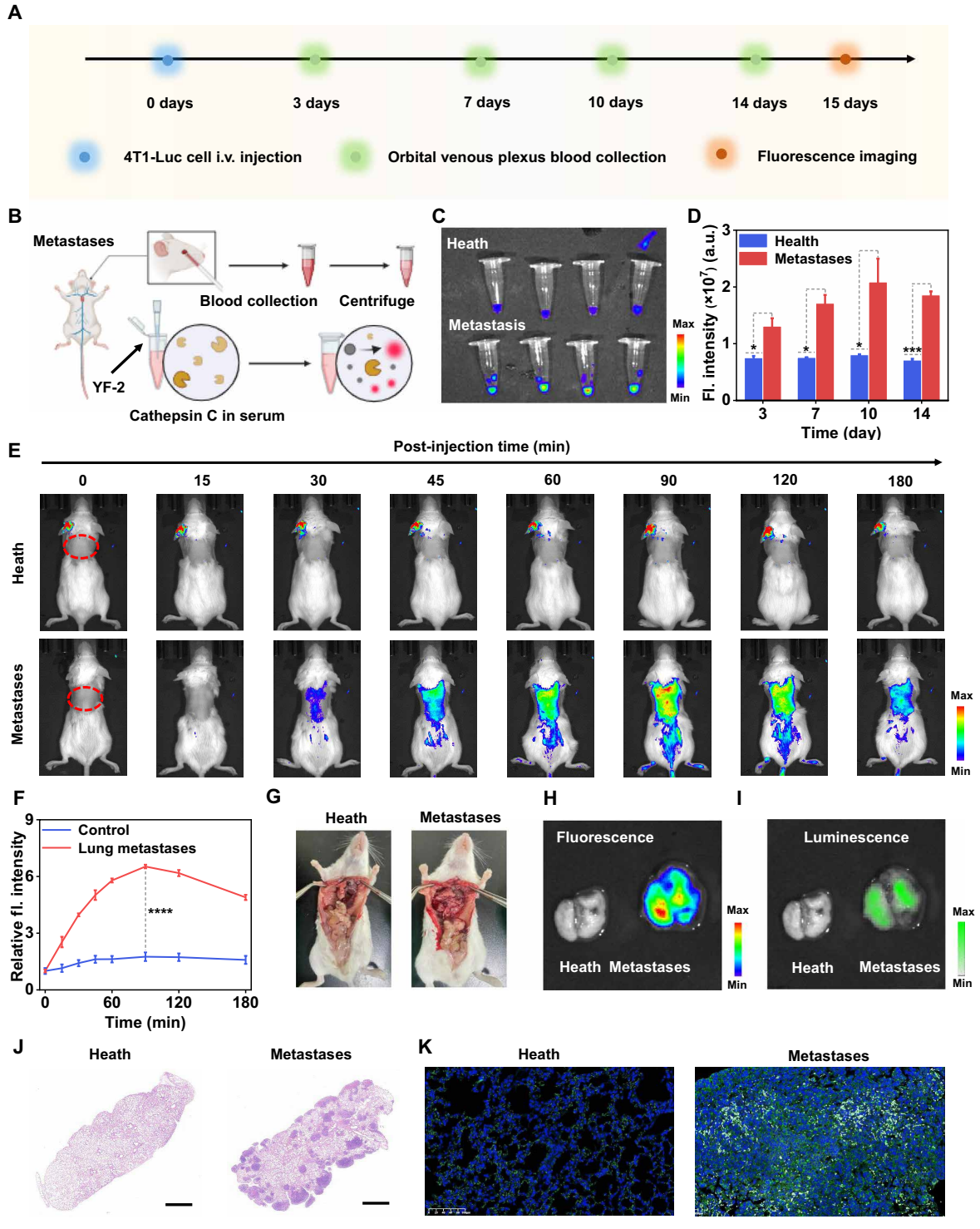

Fig. 6. Application of YF-2 in diagnosis of breast cancer lung metastases. (**A**) Schematic illustration of establishing mice models bearing lung 4T1 metastasis and the workflows for imaging/blood analysis in living mice. (**B**) Schematic illustration of YF-2 sensing mechanism in the serum from metastatic tumor mice. (**C**) Fluorescence imaging of mouse serum of mice models with varying degrees of metastasis after incubated with YF-2 (20 μM, 10 μl). (**D**) Quantitative fluorescence intensity in (B). (**E**) Representative fluorescence images of living mice after injection of YF-2 via the tail vein at different post-treatment time points. (**F**) Dynamic fluorescence intensities of lung as a function of time post-injection of YF-2 in the healthy mice and the metastasis-bearing mice. (**G**) Dissected healthy mice and metastasis-bearing mice. Representative fluorescence (**H**) and bioluminescence images (**I**) of lungs from the healthy mice and the metastasis-bearing mice at 180 min post-injection of YF-2. (**J**) H&E staining of lung tissues from the healthy mice and the metastasis-bearing mice. Scale bars, 1 mm. (**K**) Immunofluorescence analysis for evaluating CTSC activity in lung tissues from the healthy mice and the metastasis-bearing mice. Error bars, ± SEM. $n = 3$. *$P < 0.05$, ***$P < 0.001$, and ****$P < 0.0001$.

and H&E staining exhibited the formation of numerous metastases in the lungs (Fig. 6, G and J). These results demonstrated that YF-2 could be activated by the overexpressed CTSC in lung metastases, which was further confirmed by the excellent colocalization of immunofluorescence of CTSC with the fluorescence of the activated YF-2 (Fig. 6K) and the identical distribution of fluorescence and bioluminescence signals in isolated lungs (Fig. 6, H and I). Furthermore, we established mice models bearing orthotopic breast tumors. YF-2 was injected into the mice via the tail vein, followed by noninvasive in vivo imaging. The orthotopic 4T1 tumors exhibited gradually enhanced fluorescence signals with the extension of time, while there were only dim fluorescence signals in normal breasts. The fluorescence intensity ratio reached nearly fourfold between the orthotopic 4T1 tumors and normal mammary glands after 4 hours post-injection of YF-2 (fig. S28). Meanwhile, these results were also reconfirmed in mice models of orthotopic breast cancer lung metastasis (fig. S29). Thus, YF-2 was a potentially available tool for diagnosing and imaging lung metastasis of breast cancer (*38*, *64*, *65*).

DISCUSSION

Here, we reported a CTSC-activated NIRF probe (YF-1) based on the high metastasis tendency of malignant breast tumors. YF-1 specifically unlocked its NIRF signal at 715 nm by more than 20-fold in the presence of CTSC and could effectively identify malignant tumor cell lines with overexpressed CTSC (4T1 and MDA-LM2). The high signal specificity allowed the probe to distinguish the malignant and benign tumor tissues and reflect the malignancy level of tumor tissues. Moreover, the probe could accurately identify malignant breast tumor tissues of humans in a blind study. The diagnosis results given by fluorescence imaging matched perfectly with the H&E staining results, which proved that YF-1 is of potential value in the preoperatively rapid diagnosis of malignant breast tumors. Further, we synthesized a series of CTSC-activated fluorescence probes spanning visible to NIR light regions. These probes exhibited a similar capability to identify malignant breast tumor tissues with YF-1, suggesting that CTSC could be the specifically overexpressed substrate of malignant breast tumors. In addition, we further introduced PEG-2000 into YF-1 and synthesized a self-assembled nanoprobe (YF-2). This modification relieved the enrichment of the probe in the liver while maintaining excellent responsiveness. Leveraging YF-2, we visualized lung metastasis of malignant breast tumors and demonstrated that the serum CTSC activity is elevated along with the increasing metastasis of malignant breast tumors. The nanoprobe has broken through the tumor-enriching limitation of YF-1 and has great application prospects for noninvasively auxiliary evaluation of malignant breast tumor metastasis.

Despite the technological advances of these CTSC-activated probes, there are still some issues that require further research. First, the diagnostic accuracy of YF-1 in the carcinomatous features of breast tumor tissue blocks was insufficient, which could be due to the apparent differences in the penetration capability of YF-1 in the different tissue blocks. One possible solution is to develop CTSC-activated probes with high permeability. Second, YF-2 has a fast metabolic rate, which produces obstacles for tracking the metastatic process of malignant breast tumors over a long period. The limitation could be addressed by introducing the near-labeling strategy into the design of CTSC-activated probes, which allows the unlocked probe (dye) to be covalently labeled at the lesion location, enabling long-term tracking of both in situ tumors and metastases.

Studies on the physiological and pathological function of CTSC are still in the shallow stage. The CTSC-involved signaling pathways in the metastasis process of malignant breast tumor require to be systematically researched. The role of CTSC in various other diseases needs to be elucidated. In addition, the penetration depth and the variation of fluorescence signals generated by the current CTSC probes are still inadequate, which decreases the sensitivity of probes in deep tissue imaging. Long-wavelength CTSC fluorescence probes with high sensitivity or multimodal CTSC probes combined with other imaging techniques should be developed for the accurate detection of CTSC activity in deep tissues.

MATERIALS AND METHODS

Detailed synthesis procedures and spectroscopic data of all compounds are provided in the Supplementary Materials.

Materials and general methods

Unless otherwise stated, all chemical and biological reagents were analytical grade, purchased from commercial suppliers—including Beyotime Biotechnology, Sigma-Aldrich, Bide Pharmaceutical Technology, Tansoole, and Shanghai Haohong Scientific Co. Ltd. (TLC Silica Gel 60 GF254)—and used without further purification. CTSC was purchased from Sigma-Aldrich (Shanghai) Trading Co. Ltd. Cathepsin D, Cathepsin K, and Cathepsin S were purchased from MedChemExpress LLC. CTSC antibody (D-6) was purchased from Santa Cruz Biotechnology (Shanghai) Co., Ltd. MDA-231-LM2 cells were purchased from Shanghai Guandao Biological Engineering Co. Ltd. All tests are performed at room temperature. ^{1}H and ^{13}C nuclear magnetic resonance spectra were recorded on a Bruker DRX-400 spectrometer. Mass spectra were recorded on a matrix-assisted laser desorption ionization time of flight mass spectrometry (ultrafleXtreme) or LCQ Advantage ion trap mass spectrometer from Thermo Finnigan or Agilent 1100 high-performance liquid chromatography/MS.E.M. spectrometer. Ultraviolet (UV) absorption and emission spectra were recorded on UV-1800 spectrophotometer (Shimadzu Corporation, Japan) and Edinburgh spectrofluorometer, respectively. Confocal microscopy was performed on a Nikon A1 plus confocal microscope. The in vivo (living mice) imaging was carried out using an IVIS Lumina XR (IS1241N6071) in vivo imaging system.

Ethical license

All animal procedures were performed in accordance with the Regulations on experimental animals in Hunan province [license number: SYXK (Xiang) 2020-0017], and all animal experiments were approved by the Animal Ethics Committee of Hunan Provincial People's Hospital (The First Affiliated Hospital of Hunan Normal University) (number: 2023-62).

The study was approved by the Ethics Committee of Hunan Provincial People's Hospital (The First Affiliated Hospital of Hunan Normal University) (number: 2023-139), and all clinical samples were used in accordance with institutional guidelines and the Declaration of Helsinki after obtaining signed informed consent from all participants.

Benign/malignant tumor mouse model

To generate the model of breast hyperplasia mice, female balb/c mice were randomly selected and treated with estradiol benzoate (0.8 mg/kg per 2d, intraperitoneal injection, 10 times), then progesterone (4 mg/kg

per 2 days, intraperitoneal injection, four times). Female balb/c mice were randomly selected and injected with 5×10^5 4T1-Luc cells in 30 μl of Dulbecco's PBS into the right third pair of breast fat pads.

Frozen tissue section preparation

The specimens were immersed in a gel-like medium consisting of polyethylene glycol and poly (vinyl alcohol) [optimal cutting temperature compound (OCT) gel]. Each sample was rapidly frozen to about −20° to −30°C. Then, the OCT was removed to make the section of the specimen visible. The frozen tissues were cut into 20 μm for the following experiments. All of the frozen tissue sections were fixed in 75% alcohol for 1 min and then incubated directly with YF-1 (20 μM) for 20 min at room temperature. All of the sections were washed with buffer three times for each step.

Real-time in vivo NIRF imaging of lung metastasis in living mice

Real-time NIRF imaging were conducted at $t = 0$, 15, 30, 45, 60, 90, 120, or 150 min after intravenous injection of YF-2 (200 μM, 100 μl). Fluorescence images were acquired using the IVIS Lumina XR with the excitation at 710 ± 10 nm, the emission at 820 ± 10 nm, and the acquisition time of 5 s. NIRF intensities of lung in living mice were analyzed by the ROI analysis using the Living Image 4.3 Software. Mice were euthanized after live imaging. Lung tissues were collected and placed in 4% paraformaldehyde for histological examination.

Supplementary Materials

This PDF file includes:

Supplementary Text
Figs. S1 to S57
Table S1

REFERENCES AND NOTES

1. H. Sung, J. Ferlay, R. L. Siegel, M. Laversanne, I. Soerjomataram, A. Jemal, F. Bray, Global Cancer Statistics 2020: GLOBOCAN estimates of incidence and mortality worldwide for 36 cancers in 185 countries. *CA Cancer J. Clin.* **71**, 209–249 (2021).
2. S. McPhail, R. Swann, S. A. Johnson, M. E. Barclay, H. A. Elkader, R. Alvi, A. Barisic, O. Bucher, G. R. C. Clark, N. Creighton, B. Danckert, C. A. Denny, D. W. Donnelly, J. J. Dowden, N. Finn, C. R. Fox, S. Fung, A. T. Gavin, E. G. Navas, S. Habbous, J. Han, D. W. Huws, C. G. C. A. Jackson, H. Jensen, B. Kaposhi, S. E. Kumar, A. L. Little, S. Lu, C. A. McClure, B. Møller, G. Musto, Y. Nilssen, N. Saint-Jacques, S. Sarker, L. te Marvelde, R. S. Thomas, R. J. S. Thomas, C. S. Thomson, R. R. Woods, B. Zhang, G. Lyratzopoulos, B. Filsinger, K. Forster, L. May, D. S. Morrison, A. F. Thomas, J. L. Warlow, H. You, Risk factors and prognostic implications of diagnosis of cancer within 30 days after an emergency hospital admission (emergency presentation): An International Cancer Benchmarking Partnership (ICBP) population-based study. *Lancet Oncol.* **23**, 587–600 (2022).
3. K. L. Britt, J. Cuzick, K.-A. Phillips, Key steps for effective breast cancer prevention. *Nat. Rev. Cancer* **20**, 417–436 (2020).
4. E. Nolan, G. J. Lindeman, J. E. Visvader, Deciphering breast cancer: from biology to the clinic. *Cell* **186**, 1708–1728 (2023).
5. W. Chen, A. D. Hoffmann, H. Liu, X. Liu, Organotropism: New insights into molecular mechanisms of breast cancer metastasis. *npj Precis. Oncol.* **2**, 4 (2018).
6. G. P. Gupta, J. Massagué, Cancer metastasis: Building a framework. *Cell* **127**, 679–695 (2006).
7. F. Bertucci, C. K. Y. Ng, A. Patsouris, N. Droin, S. Piscuoglio, N. Carbuccia, J. C. Soria, A. T. Dien, Y. Adnani, M. Kamal, S. Garnier, G. Meurice, M. Jimenez, S. Dogan, B. Verret, M. Chaffanet, T. Bachelot, M. Campone, C. Lefeuvre, H. Bonnefoi, F. Dalenc, A. Jacquet, M. R. De Filippo, N. Babbar, D. Birnbaum, T. Filleron, C. Le Tourneau, F. André, Genomic characterization of metastatic breast cancers. *Nature* **569**, 560–564 (2019).
8. B. Verret, M. Bottosso, S. Hervais, B. Pistilli, The molecular predictive and prognostic biomarkers in metastatic breast cancer: The contribution of molecular profiling. *Cancer* **14**, 4203 (2022).
9. D. Crosby, S. Bhatia, K. M. Brindle, L. M. Coussens, C. Dive, M. Emberton, S. Esener, R. C. Fitzgerald, S. S. Gambhir, P. Kuhn, T. R. Rebbeck, S. Balasubramanian, Early detection of cancer. *Science* **375**, eaay9040 (2022).
10. J. Chi, Y. Xue, Y. Zhou, T. Han, B. Ning, L. Cheng, H. Xie, H. Wang, W. Wang, Q. Meng, K. Fan, F. Gong, J. Fan, N. Jiang, Z. Liu, K. Pan, H. Sun, J. Zhang, Q. Zheng, J. Wang, M. Su, Y. Song, Perovskite Probe-Based Machine Learning Imaging Model for Rapid Pathologic Diagnosis of Cancers. *ACS Nano* **18**, 24295–24305 (2024).
11. L. Nicosia, A. C. Bozzini, S. Palma, M. Montesano, F. Pesapane, F. Ferrari, V. Dominelli, A. Rotili, L. Meneghetti, S. Frassoni, V. Bagnardi, C. Sangalli, E. Cassano, A Score to Predict the Malignancy of a Breast Lesion Based on Different Contrast Enhancement Patterns in Contrast-Enhanced Spectral Mammography. *Cancer* **14**, 4337 (2022).
12. S. Wang, Y. Sun, R. Li, N. Mao, Q. Li, T. Jiang, Q. Chen, S. Duan, H. Xie, Y. Gu, Diagnostic performance of perilesional radiomics analysis of contrast-enhanced mammography for the differentiation of benign and malignant breast lesions. *Eur. Radiol.* **32**, 639–649 (2021).
13. J. E. Kalinyak, W. A. Berg, K. Schilling, K. S. Madsen, D. Narayanan, M. Tartar, Breast cancer detection using high-resolution breast PET compared to whole-body PET or PET/CT. *Eur. J. Nucl. Med. Mol. Imaging* **41**, 260–275 (2013).
14. H. Brar, L. Hogen, A. Covens, Cost-effectiveness of sentinel node biopsy and pathological ultrastaging in patients with early-stage cervical cancer. *Cancer* **123**, 1751–1759 (2017).
15. Y. Zhan, S. Ling, H. Huang, Y. Zhang, G. Chen, S. Huang, C. Li, W. Guo, Q. Wang, Rapid unperturbed-tissue analysis for intraoperative cancer diagnosis using an enzyme-activated NIR-II nanoprobe. *Angew. Chem. Int. Ed. Engl.* **60**, 2637–2642 (2020).
16. K. Kobayashi, K. Ando, K. Ito, M. Tsushima, M. Morozumi, S. Tanaka, M. Machino, K. Ota, N. Ishiguro, S. Imagama, Accuracy of intraoperative pathological diagnosis using frozen sections of spinal cord lesions. *Clin. Neurol. Neurosurg.* **167**, 117–121 (2018).
17. Y. Zhang, G. Zhang, Z. Zeng, K. Pu, Activatable molecular probes for fluorescence-guided surgery, endoscopy and tissue biopsy. *Chem. Soc. Rev.* **51**, 566–593 (2022).
18. N. Houssami, P. Macaskill, M. L. Marinovich, M. Morrow, The association of surgical margins and local recurrence in women with early-stage invasive breast cancer treated with breast-conserving therapy: A meta-analysis. *Ann. Surg. Oncol.* **21**, 717–730 (2014).
19. H. O. Kobayashi, M. Ogawa, R. Alford, P. L. Choyke, Y. Urano, New strategies for fluorescent probe design in medical diagnostic imaging. *Chem. Rev.* **110**, 2620–2640 (2010).
20. M. Gao, F. Yu, C. Lv, J. Choo, L. Chen, Fluorescent chemical probes for accurate tumor diagnosis and targeting therapy. *Chem. Soc. Rev.* **46**, 2237–2271 (2017).
21. G. Jiang, H. Liu, G. Deng, H. Liu, Z. Zhou, T. B. Ren, L. Wang, X. B. Zhang, L. Yuan, "Zero" intrinsic fluorescence sensing-platforms enable ultrasensitive whole blood diagnosis and in vivo imaging. *Angew. Chem. Int. Ed. Engl.* **63**, e202400637 (2024).
22. Z. Qin, T. B. Ren, H. Zhou, X. Zhang, L. He, Z. Li, X. B. Zhang, L. Yuan, NIR II-HDs: A versatile platform for developing activatable NIR-II fluorogenic probes for reliable in vivo analyte sensing. *Angew. Chem. Int. Ed. Engl.* **61**, e2022015 (2022).
23. M. Y. Lucero, Y. Tang, C. J. Zhang, S. Su, J. A. Forzano, V. Garcia, X. Huang, D. Moreno, J. Chan, Activity-based photoacoustic probe for biopsy-free assessment of copper in murine models of Wilson's disease and liver metastasis. *Proc. Natl. Acad. Sci. U.S.A.* **118**, e2106943118 (2021).
24. Y. Kuriki, T. Yoshioka, M. Kamiya, T. Komatsu, H. Takamaru, K. Fujita, H. Iwaki, A. Nanjo, Y. Akagi, K. Takeshita, H. Hino, R. Hino, R. Kojima, T. Ueno, K. Hanaoka, S. Abe, Y. Saito, J. Nakajima, Y. Urano, Development of a fluorescent probe library enabling efficient screening of tumour-imaging probes based on discovery of biomarker enzymatic activities. *Chem. Sci.* **13**, 4474–4481 (2022).
25. B. Zhang, J. Lu, X. Lin, J. Wang, Q. Li, T. Jin, Q. Shi, Y. Lu, J. Zhang, J. Deng, Y. Zhang, Y. Guo, J. Gao, H. Chen, Y. Yan, J. Wu, J. Gao, J. Che, X. Dong, Z. Gu, N. Lin, Injectable and Sprayable Fluorescent Nanoprobe for Rapid Real-Time Detection of Human Colorectal Tumors. *Adv. Mater.* **36**, 2405275 (2024).
26. Z. Zeng, S. S. Liew, X. Wei, K. Pu, Hemicyanine-based near-infrared activatable probes for imaging and diagnosis of diseases. *Angew. Chem. Int. Ed. Engl.* **60**, 26454–26475 (2021).
27. H. Li, D. Kim, Q. Yao, H. Ge, J. Chung, J. Fan, J. Wang, X. Peng, J. Yoon, Activity-based NIR enzyme fluorescent probes for the diagnosis of tumors and image-guided surgery. *Angew. Chem. Int. Ed. Engl.* **60**, 17268–17289 (2021).
28. X. Zhen, X. Jiang, Polymer-based activatable optical probes for tumor fluorescence and photoacoustic imaging. *Wiley Interdiscip. Rev. Nanomed. Nanobiotechnol.* **12**, e1593 (2019).
29. J. Mei, H. Tian, Most recent advances on enzyme-activatable optical probes for bioimaging. *Aggregate* **2**, e32 (2021).
30. W. Z. W. Li, X. Q. Liu, L.-R. Liu, J. Xiao, X. Q. Wang, Y.-Y. Ye, Z.-X. Wang, M.-Y. Zhu, Y. Sun, P. J. Stang, Y. Sun, Supramolecular coordination platinum metallacycle–based multilevel wound dressing for bacteria sensing and wound healing. *Proc. Natl. Acad. Sci. U.S.A.* **121**, e2318391121 (2024).
31. H. Iwashita, E. Castillo, M. S. Messina, R. A. Swanson, C. J. Chang, A tandem activity-based sensing and labeling strategy enables imaging of transcellular hydrogen peroxide signaling. *Proc. Natl. Acad. Sci. U.S.A.* **118**, e2018513118 (2021).
32. D. G. J. Linders, O. D. Bijlstra, L. C. Fallert, D. E. Hilling, E. Walker, B. Straight, T. L. March, A. R. P. M. Valentijn, M. Pool, J. Burggraaf, J. P. Basilion, A. L. Vahrmeijer, P. J. K. Kuppen, Cysteine cathepsins in breast cancer: Promising targets for fluorescence-guided surgery. *Mol. Imaging Biol.* **25**, 58–73 (2022).

33. D. Kato, K. M. Boatright, A. B. Berger, T. Nazif, G. Blum, C. Ryan, K. A. H. Chehade, G. S. Salvesen, M. Bogyo, Activity-based probes that target diverse cysteine protease families. *Nat. Chem. Biol.* **1**, 33–38 (2005).
34. J. A. Joyce, A. Baruch, K. Chehade, N. Meyer-Morse, E. Giraudo, F.-Y. Tsai, D. C. Greenbaum, J. H. Hager, M. Bogyo, D. Hanahan, Cathepsin cysteine proteases are effectors of invasive growth and angiogenesis during multistage tumorigenesis. *Cancer Cell* **5**, 443–453 (2001).
35. M. M. Mohamed, B. F. Sloane, multifunctional enzymes in cancer. *Nat. Rev. Cancer* **6**, 764–775 (2006).
36. B. Ruffell, N. I. Affara, L. Cottone, S. Junankar, M. Johansson, D. G. DeNardo, L. Korets, T. Reinheckel, B. F. Sloane, M. Bogyo, L. M. Coussens, Cathepsin C is a tissue-specific regulator of squamous carcinogenesis. *Genes Dev.* **27**, 2086–2098 (2013).
37. Y. Xiao, M. Cong, J. Li, D. He, Q. Wu, P. Tian, Y. Wang, S. Yang, C. Liang, Y. Liang, J. Wen, Y. Liu, W. Luo, X. Lv, Y. He, D.-D. Cheng, T. Zhou, W. Zhao, P. Zhang, X. Zhang, Y. Xiao, Y. Qian, H. Wang, Q. Gao, Q.-C. Yang, Q. Yang, G. Hu, Cathepsin C promotes breast cancer lung metastasis by modulating neutrophil infiltration and neutrophil extracellular trap formation. *Cancer Cell* **39**, 423–437.e7 (2021).
38. L. Yuan, W. Lin, S. Zhao, W. Gao, B. Chen, L. He, S. Zhu, A Unique Approach to Development of Near-Infrared Fluorescent Sensors for in Vivo Imaging. *J. Am. Chem. Soc.* **134**, 13510–13523 (2012).
39. S. Zuo, G. Jiang, Y. Zheng, X. Zhang, Z. Qin, L. Chen, T. Ren, X.-B. Zhang, L. Yuan, Family of hNQO1 activatable near-infrared fluoro-photoacoustic probes for diagnosis of wound infection and ulcerative colitis. *Anal. Chem.* **95**, 898–906 (2023).
40. M. P. Jewgiński, M. Makowski, M. Pawełczak, W. Goldeman, A. Trojanowska-Laskowska, P. Kafarski, R. Latajka, Synthesis of Hybrid Tripeptide Peptidomimetics Containing Dehydroamino Acid and Aminophosphonic Acid in the Chain and Evaluation of Their Activity toward Cathepsin C. *Chem. Biodivers.* **19**, e202101019 (2022).
41. M. S. B. Khan, M. H. Baig, S. Ahmad, S. A. Siddiqui, A. K. Srivastava, K. V. Srinivasan, I. A. Ansari, Design, synthesis, evaluation and thermodynamics of 1- substituted pyridylimidazo[1,5-a]pyridine derivatives as cysteine protease inhibitors. *PLOS ONE* **8**, e69982 (2013).
42. H. Li, Q. Yao, W. Sun, K. Shao, Y. Lu, J. Chung, D. Kim, J. Fan, S. Long, J. Du, Y. Li, J. Wang, J. Yoon, X. Peng, Aminopeptidase N activatable fluorescent probe for tracking metastatic cancer and image-guided surgery via in situ spraying. *J. Am. Chem. Soc.* **142**, 6381–6389 (2020).
43. Q. Lan, P. Yu, K. Yan, X. Li, F. Zhang, Z. Lei, Polymethine molecular platform for ratiometric fluorescent probes in the second near-infrared window. *J. Am. Chem. Soc.* **144**, 21010–21015 (2022).
44. H. Mao, Y. Cao, Z. Zou, J. Xia, J. Zhao, An enzyme-powered microRNA discriminator for the subtype-specific diagnosis of breast cancer. *Chem. Sci.* **14**, 2097–2106 (2023).
45. J. Z. Bange, E. Ullrich, A. Ullrich, Molecular targets for breast cancer therapy and prevention. *Nat. Med.* **7**, 548–552 (2001).
46. D. Asanuma, M. Sakabe, M. Kamiya, K. Yamamoto, J. Hiratake, M. Ogawa, N. Kosaka, P. L. Choyke, T. Nagano, H. Kobayashi, Y. Urano, Sensitive β-galactosidase-targeting fluorescence probe for visualizing small peritoneal metastatic tumours in vivo. *Nat. Commun.* **6**, 6463 (2015).
47. A. Mochida, F. Ogata, T. Nagaya, P. L. Choyke, H. Kobayashi, Activatable fluorescent probes in fluorescence-guided surgery: Practical considerations. *Bioorg. Med. Chem.* **26**, 925–930 (2018).
48. E. J. Schneble, L. J. Graham, M. P. Shupe, F. L. Flynt, K. P. Banks, A. D. Kirkpatrick, A. Nissan, L. Henry, A. Stojadinovic, N. M. Shumway, I. Avital, G. E. Peoples, R. F. Setlik, Current approaches and challenges in early detection of breast cancer recurrence. *J. Cancer* **5**, 281–290 (2014).
49. C. Yang, C. Jiang, M. Yang, Q. Bai, Y. Zhen, Y. Zhang, W. Yin, J. Wang, X. Zhou, G. Li, M. Wu, Y. Qin, Q. Wang, H. Ji, L. Wu, NAD(P)H activated fluorescent probe for rapid intraoperative pathological diagnosis and tumor histological grading. *Chem. Biomed. Imaging* **1**, 738–749 (2023).
50. A.-A. Storms, P. Sukumvanich, S. E. Monaco, S. Beriwal, T. C. Krivak, A. B. Olawaiye, A. Kanbour-Shakir, Mucinous tumors of the ovary: Diagnostic challenges at frozen section and clinical implications. *Gynecol. Oncol.* **125**, 75–79 (2012).
51. K. Fujita, M. Kamiya, T. Yoshioka, A. Ogasawara, R. Hino, R. Kojima, H. Ueo, Y. Urano, Rapid and Accurate Visualization of Breast Tumors with a Fluorescent Probe Targeting α-Mannosidase 2C1. *ACS Cent. Sci.* **6**, 2217–2227 (2020).
52. S. Wei, Update on selective special types of breast neoplasms: Focusing on controversies, differential diagnosis, and molecular genetic advances. *Semin. Diagn. Pathol.* **39**, 367–379 (2022).
53. K. N. Ogston, I. D. Miller, S. Payne, A. W. Hutcheon, T. K. Sarkar, I. Smith, A. Schofield, S. D. Heys, A new histological grading system to assess response of breast cancers to primary chemotherapy: Prognostic significance and survival. *Breast* **12**, 320–327 (2003).
54. Y. J. Yang, M. Dai, Y. J. Reo, C. W. Song, S. Sarkar, K. H. Ahn, NAD(P)H quinone oxidoreductase-1 in organ and tumor tissues: Distinct activity levels observed with a benzo-rosol-based dual-excitation and dual-emission probe. *Anal. Chem.* **93**, 7523–7531 (2021).
55. Q. Wu, Q.-H. Zhou, W. Li, T.-B. Ren, X.-B. Zhang, L. Yuan, Evolving an ultra-sensitive near-infrared β-galactosidase fluorescent probe for breast cancer imaging and surgical resection navigation. *ACS Sens.* **7**, 3829–3837 (2022).
56. D. Hanahan, R. A. Weinberg, The hallmarks of cancer. *Cell* **100**, 57–70 (2000).
57. D. Entenberg, M. H. Oktay, J. S. Condeelis, Intravital imaging to study cancer progression and metastasis. *Nat. Rev. Cancer* **23**, 25–42 (2023).
58. C. Andreou, R. Weissleder, M. F. Kircher, Multiplexed imaging in oncology. *Nat. Biomed. Eng.* **6**, 527–540 (2022).
59. L. Jin, B. Han, E. Siegel, Y. Cui, A. Giuliano, X. Cui, Breast cancer lung metastasis: Molecular biology and therapeutic implications. *Cancer Biol. Ther.* **19**, 858–868 (2018).
60. H. Lee, W. Akers, K. Bhushan, S. Bloch, G. Sudlow, R. Tang, S. Achilefu, Near-infrared pH-activatable fluorescent probes for imaging primary and metastatic breast tumors. *Bioconjug. Chem.* **22**, 777–784 (2011).
61. H. Xiong, H. Zuo, Y. Yan, G. Occhialini, K. Zhou, Y. Wan, D. J. Siegwart, High-contrast fluorescence detection of metastatic breast cancer including bone and liver micrometastases via size-controlled pH-activatable water-soluble probes. *Adv. Mater.* **29**, 1700131 (2017).
62. Y. Zhou, L. Zhu, B. Liu, W. Xu, X. Yang, Y. Liu, B. Ruan, S. Yi, B. Liang, G. Dong, J. Huang, Tailored zwitterionic hemicyanine reporters for early diagnosis and prognostic assessment of acute renal failure. *Angew. Chem. Int. Ed. Engl.* **62**, e2023154 (2023).
63. X. Zhuang, H. Zhang, X. Li, X. Li, M. Cong, F. Peng, J. Yu, X. Zhang, Q. Yang, G. Hu, Differential effects on lung and bone metastasis of breast cancer by Wnt signalling inhibitor DKK1. *Nat. Cell Biol.* **19**, 1274–1285 (2017).
64. S. He, J. Li, Y. Lyu, J. Huang, K. Pu, Near-infrared fluorescent macromolecular reporters for real-time imaging and urinalysis of cancer immunotherapy. *J. Am. Chem. Soc.* **142**, 7075–7082 (2020).
65. K. Fujita, Y. Urano, Activity-based fluorescence diagnostics for cancer. *Chem. Rev.* **124**, 4021–4078 (2024).

Acknowledgments

Funding: This work was supported by National Natural Science Foundation of China [no. 22325401 (to L.Y.), no. 22074036 (to L.Y.), no. 22374039 (to T.-B.R.), and no. 22404052 (to G.J.)], the Science and Technology Project of Hunan Province [no. 2021RC4021 (to L.Y.) and no. 2024RC3089 (to G.J.)], the China Postdoctoral Science Foundation [no. 2024 M750859 (to G.J.)], the National Postdoctoral Program for Innovative Talents [no. BX20230113 (to G.J.)], and the Natural Science Foundation of Hunan Province [no. 2023JJ20004 (to T.-B.R.)]. **Author contributions:** Conceptualization: L.Y., G.J., S.Z., T.-B.R., L.C., and Y.C. Methodology: Y.L., S.Z., G.J., S.H., L.Y., Y.C., T.-B.R., and L.C. Treatment protocol: S.Z., G.J., L.Y., S.H., Y.L., Z.Z., Y.C., L.C., and X.-B.Z. Data analysis: L.Y., S.Z., G.J., S.H., Y.L., Z.Z., Y.C., T.-B.R., L.C., X.-B.Z., and S.L. Writing—original draft: S.Z., G.J., L.Y., S.H., Y.L., Y.C., L.C., X.-B.Z., and S.L. Writing—review and editing: G.J., S.Z., L.Y., S.H., Y.L., Z.Z., T.-B.R., L.C., X.-B.Z., and S.L. **Competing interests:** L.Y., S.Z., G.J., and X.-B.Z. are inventors on a pending patent related to this work filed by Hunan University. The other authors declare that they have no competing interests. **Data and materials availability:** All data needed to evaluate the conclusions in the paper are present in the paper and/or the Supplementary Materials.

Submitted 6 July 2024
Accepted 27 February 2025
Published 2 April 2025
10.1126/sciadv.adr5541